SANDIA REPORT
SAND2022-XXXX
Printed May 2022

Sandia National Laboratories

Unraveling the Wrinkle in Time-Variable Sources with Lunes and Synthetic Seismic Data

Elizabeth Berg & Christian Poppeliers

Prepared by
Sandia National Laboratories
Albuquerque, New Mexico 87185
Livermore, California 94550

Issued by Sandia National Laboratories, operated for the United States Department of Energy by National Technology & Engineering Solutions of Sandia, LLC.

Available to DOE and DOE contractors from

U.S. Department of Energy
Office of Scientific and Technical Information
P.O. Box 62
Oak Ridge, TN 37831

Telephone: (865) 576-8401
Facsimile: (865) 576-5728
E-Mail: reports@osti.gov
Online ordering: http://www.osti.gov/scitech

Available to the public from

U.S. Department of Commerce
National Technical Information Service
5301 Shawnee Road
Alexandria, VA 22312

Telephone: (800) 553-6847
Facsimile: (703) 605-6900
E-Mail: orders@ntis.gov
Online order: https://classic.ntis.gov/help/order-methods

ABSTRACT

In this report, we describe how to estimate the time-variable components of the seismic moment tensor and compare these estimates to the more conventional analysis that incorporates an assumption of the source time function (STF) across all components of the seismic moment tensor. The advantage of our method is that we are able to independently estimate the time-evolution of each component of the seismic moment tensor, which may help to resolve the complex source phenomena associated with buried explosions. By performing an eigen decomposition of the time-evolving seismic moment tensor components, we are able to plot the seismic mechanism as a trajectory on a lune diagram. This technique enables interpretation of the seismic mechanism as a function of time, as opposed to the more conventional analysis which assumes that the seismic mechanism is time invariant. Finally, we describe the differences between the seismic moment and the seismic moment rate STFs, how to implement each one in inversion schemes, and the relative strengths/weaknesses of each. Our key take-away is that we are able to distinguish nearly-overlapping sources with highly different mechanisms, such as an explosion immediately following an earthquake, by estimating moment rate from seismic data through a STF-invariant inversion for the full time-variable moment tensor.

ACKNOWLEDGMENT

This research was funded by the National Nuclear Security Administration, Defense Nuclear Nonproliferation Research and Development (NNSA DNN R&D). The Source Physics Experiments (SPE) would not have been possible without the support of many people from several organizations. The authors wish to express their gratitude to the (NNSA DNN R&D), and the SPE working group, a multi-institutional and interdisciplinary group of scientists and engineers. We also thank Brian Young for his insight and constructive feedback to our study. Sandia National Laboratories is a multimission laboratory managed and operated by National Technology & Engineering Solutions of Sandia, LLC, a wholly owned subsidiary of Honeywell International Inc., for the U.S. Department of Energy's National Nuclear Security Administration under contract DE-NA0003525.

CONTENTS

LIST OF FIGURES

SUMMARY

This work describes the formulation and visualization, via lunes and beachball graphics, for moment and moment rate source-time functions from local-scale synthetic seismic data and the utility of each.

1. FORWARD LINEAR MODEL OF SEISMIC WAVES

In this chapter, we present the linear forward model of seismic waves, including discussion of source functions in terms of moment versus moment rate. Next, we discuss the specifics of both explosion and earthquake source-time functions and how these source types can be visualized through classic 'beachball' graphics and on a fundamental lune.

1.1. Basic Review of Seismic Signals

We model far-field seismic waves as

$$u_k(\mathbf{x}',t') = \sum_{n=1}^{N} \int_{-\infty}^{\infty} \int_{V_0} g_{k,n}(\mathbf{x}',t;\mathbf{x},t) S_n(\mathbf{x},t) dV dt. \tag{1.1}$$

where the seismic wavefield u observed in the far-field at station k, located at $\mathbf{x}' = [x',y',z']$, is the convolution of a series seismic sources, $S_n(\mathbf{x},t)$ with their corresponding Green's functions, $g(\mathbf{x}';\mathbf{x},t)$. The seismic source consist of N term located at the source region $\mathbf{x} = [x,y,z]$. The corresponding Green's functions, $g(\mathbf{x}';\mathbf{x},t)$ describe the impulse response of the Earth to the nth source between the source region and the recording station (Aki and Richards, 2002).

For our model, we simplify the source region as an infinitely small point, and we thus rewrite equation 1.1 as:

$$u_k(\mathbf{x}',t') = \sum_{n=1}^{N} \int_{-\infty}^{\infty} g_{k,n}(\mathbf{x}',t;\mathbf{x},t) m_n(\mathbf{x},t) dt. \tag{1.2}$$

where m_n are a series of time-varying forces and/or force couples acting at source location $\mathbf{x}$. For our model, we do not require that the force couples in the moment tensor are identical. Rather, we recognize that each term in the moment tensor can have independent time histories, and thus the term $m_n(\mathbf{x},t)$ in equation 1.1 can be written as

$$m_n(\mathbf{x},t) = \begin{bmatrix} M_{xx}(\mathbf{x},t) & M_{xy}(\mathbf{x},t) & M_{xz}(\mathbf{x},t) \\ M_{yx}(\mathbf{x},t) & M_{yy}(\mathbf{x},t) & M_{yz}(\mathbf{x},t) \\ M_{zx}(\mathbf{x},t) & M_{zy}(\mathbf{x},t) & M_{zz}(\mathbf{x},t) \end{bmatrix}. \tag{1.3}$$

If the time-dependence of the force couples m_n are equal, then the terms in the moment tensor act to scale a single source-time function (STF). In other words, the force couples $m_n(\mathbf{x},t)$ of equation 1.2 can be written as the product of a source-time function and the individual scalars of the seismic moment tensor

$$m_n(\mathbf{x},t) = h(t)\hat{m}_n(\mathbf{x}) \tag{1.4}$$

where $h(t)$ can be any arbitrary function. For example, the STF is often assumed to be a step function when $h(t)$ describes moment and a Dirac delta when $h(t)$ is a moment rate function. In this case, equation 1.2 becomes

$$u_k(\mathbf{x}',t') = \sum_{n=1}^{6} \int_{-\infty}^{\infty} g_{k,n}(\mathbf{x}',t;\mathbf{x},t) h(t) \hat{m}_n(\mathbf{x}) dt \tag{1.5}$$

where

$$m_n(\mathbf{x},t) = h(t)\hat{m}_n(\mathbf{x}) = h(t) \begin{bmatrix} \hat{M}_{xx}(\mathbf{x}) & \hat{M}_{xy}(\mathbf{x}) & \hat{M}_{xz}(\mathbf{x}) \\ \hat{M}_{yx}(\mathbf{x}) & \hat{M}_{yy}(\mathbf{x}) & M_{yz}(\mathbf{x}) \\ \hat{M}_{zx}(\mathbf{x}) & \hat{M}_{zy}(\mathbf{x}) & \hat{M}_{zz}(\mathbf{x}) \end{bmatrix}. \tag{1.6}$$

Finally, we assume that there are no net torques in the seismic source. This makes the moment tensor symmetric ($M_{xy}(\mathbf{x}) = M_{yx}(\mathbf{x})$, etc.)

For the model shown in equation 1.5, the moment tensor $\hat{m}_n(\mathbf{x})$ acts to scale a single STF $h(t)$. We will refer to this model as the STF-Dependent model, which is in contrast to that of equation 1.1-1.2, which enforces no such STF similarity for the moment tensor components. In the case that data is inverted using the STF-Dependent model (and an *a priori* assumption of $h(t)$), the results are a set of scalars corresponding to the six independent terms of the moment tensor. These six scalars form a symmetric tensor and the corresponding eigen-vectors can be graphically represented as a 'beachball' graphic or a single point on the fundamental lune (Tape and Tape, 2012).

In the above formulations the STF $h(t)$ describes the moment, which is a force multiplied by distance (e.g. SI units of N m). However, there is often confusion and/or errors in the published literature regarding this term. Specifically, is $h(t)$ a "moment" or a "moment rate" function? We will define the moment rate function as the first time derivative of the moment function

$$\frac{\partial m_n(\mathbf{x},t)}{\partial t} = \frac{\partial h(t)}{\partial t}\hat{m}_n(\mathbf{x}) = \frac{\partial h(t)}{\partial t} \begin{bmatrix} \hat{M}_{xx}(\mathbf{x}) & \hat{M}_{xy}(\mathbf{x}) & \hat{M}_{xz}(\mathbf{x}) \\ \hat{M}_{yx}(\mathbf{x}) & \hat{M}_{yy}(\mathbf{x}) & M_{yz}(\mathbf{x}) \\ \hat{M}_{zx}(\mathbf{x}) & \hat{M}_{zy}(\mathbf{x}) & \hat{M}_{zz}(\mathbf{x}) \end{bmatrix}, \tag{1.7}$$

and in the next section will explicitly describe the caveats of using a moment function versus a moment rate function, the data units required for each, and the relative advantages/disadvantages of each.

1.2. Source Time Functions

To produce a seismic wavefield, mechanical energy must be injected into the Earth. This energy can be injected continuously, as in the case of ocean-generated microseism or wind-induced seismic noise, or via discrete, transient events such as an earthquake or buried explosion. For our work here, we focus on buried explosions and earthquakes. For these types of events, there exists a concept termed the source time function (STF) that models the rate and quantity of energy that is input into the Earth. The STF is a concept that simplifies the highly complex physical processes that occur in the Earth during an earthquake or explosion that result in a seismic wavefield. It is

important to point out that the STF only describes "how much" and "how fast" the energy is input into the Earth, and not "in what direction". To fully model the wavefield, the STF must be scaled by the moment tensor, which in turn models observed seismic radiation patterns. In this section, we present two common models for STFs, one for buried explosions and another for earthquakes. Finally, we present a visualization of the STFs to link the scaling of the moment tensor to the STFs.

Haskell (1967) proposed a model to describe a STF for an explosive source, in the form of reduced displacement potentials, for local scale observations in a variety of subsurface mediums as given by Werth and Herbst (1963). Assuming a spherically symmetric source and the creation of a cavity after the explosion (e.g. permanent deformation), the reduced displacement potential, $\Psi(t)$, can be modeled as

$$\Psi(t) = \Psi(\infty)(1 - e^{-kt}[1 + kt + \frac{(kt)^2}{2} + \frac{(kt)^3}{6} - B(kt)^4]) \tag{1.8}$$

where the empirical parameter B (dimensionless) describes the non-permanent overshoot and k (SI units of s^{-1}) controls the source bandwidth. Note that this model is similar to the so-called Mueller-Murphy STF for a contained explosion (Murphy, 1977; Mueller and Murphy, 1971).

The STF for an earthquake has a similar functional form as that of an explosion. However, in addition to the STF itself, the earthquake source model assumes that the energy is produced by physical slip along a fault plane with orientation given by its strike ϕ and dip δ (e.g. Ammon et al. (2020)). The direction of slip is given by the rake λ. Note that a "pure" earthquake source, termed a double couple source, implies that there is no volumetric change during the rupture process. Tanioka and Ruff (1997) give a model for a moment rate STF of a "typical" earthquake as

$$\begin{aligned} f(t) &= m(\frac{2}{d}t)^{1+\gamma} \quad \text{for } 0 \leq t \leq \frac{d}{2} \\ f(t) &= m(2 - \frac{2}{d}t)^{1+\gamma} \quad \text{for } \frac{d}{2} \leq t \leq d, \end{aligned} \tag{1.9}$$

where m is the maximum amplitude, d the total function time, and γ the function's shape. Note that this is a moment rate function, so the moment function can be determined by integrating this function with respect to time.

To visualize the time-variable STFs for both of these classical source types, we plot the simulated STFs of an explosion and earthquake for each component of the moment tensor. We graphically arrange the STFs to correspond to the component of the moment tensor, omitting the redundant symmetric terms (Figure 1-1). For both source types, the total energy of the source is 1×10^{10} N m. The explosion is purely isotropic whereas the earthquake is defined to have a strike, dip, and rake of 10°, 85°, 5°, respectively, with a total rupture time of 0.7 seconds. In panels (a) and (b) of Figure 1-1 we show the moment function and in panels (c) and (d) of the same figure we show the moment rate function.

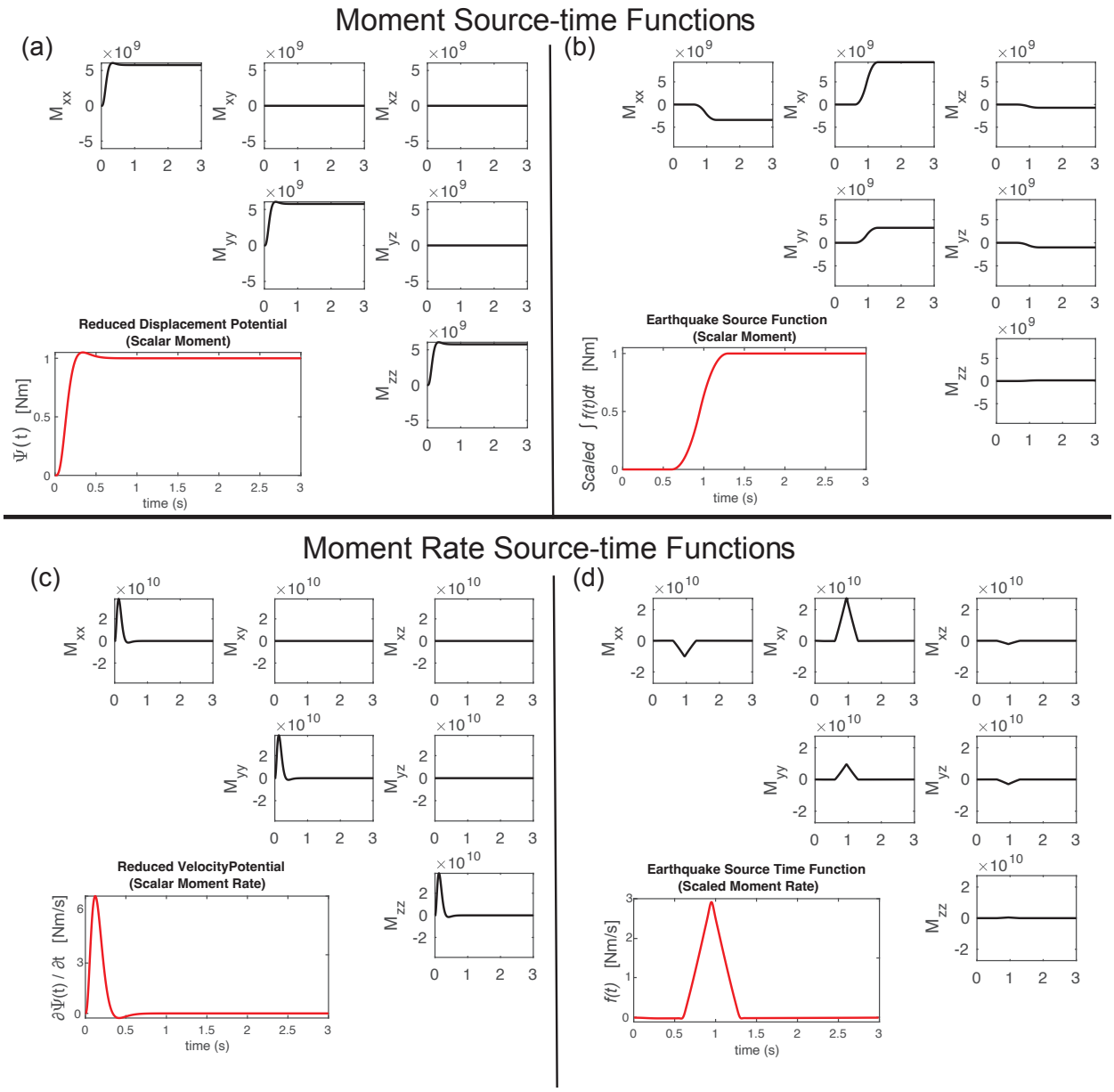

Figure 1-1. Original source time functions (red) and scaled according to the source tensor (black). The M_{ij} values are in units of N m for the source moment (top) and units of Nms^{-1} for the source moment rate (bottom). Shown are synthetics from (a) explosion moment source, (b) earthquake moment source, (c) explosion moment rate source, and (d) earthquake moment rate source.

2. SEISMIC SOURCE MECHANISMS

In current and conventional analyses of earthquake and explosion source mechanisms, the STF is assumed to be identical for all components of the moment tensor, regardless of the source mechanism or frequency content of the analysis (e.g. (Chiang et al., 2016; Ford et al., 2009; Herrmann et al., 2011; Rösler and Stein, 2022)). In this case, the moment tensor is treated as a 3×3 array of scalars which quantify the relative scale of the STF for each moment tensor component (e.g., Equation 1.6). In this model, the moment tensor can be visualized using the well known "beachball" diagrams, which show the orientation and (potentially) the mechanism of the source, or plotted on a so-called source-type plot, first introduced by Hudson et al. (1989) and more recently onto a fundamental lune Tape and Tape (2012), both of which show only the mechanism.

A source-type plot is a method by which to visualize the mechanism of a seismic point-source, assuming that the moment tensor is symmetric. For both the equal-area Hudson plots and lune plots, the fundamental idea is that a moment tensor's eigenvalues are directly linked to the relative magnitude of each moment tensor component, and thus the source type. It's important to note that a source-type plot, regardless of the flavor, assumes that the moment tensor is symmetric and that it does not convey information about the orientation or magnitude of the event.

For our work here, we will briefly review the most important concepts of the source-type plots first proposed by Tape and Tape (2012), as this type of visualization makes more sense from a geometrical standpoint: the so-called Hudson Tk plots essentially plot the source mechanism on an equal-area cube, projected onto a 2D surface, whereas the visualization introduced by Tape and Tape (2012) plots the source onto a fundamental lune with no required assumption of eigenvalue probabilities. The mathematical details of source-type plots is extensive, if not overly dense, and thus we will only summarize the most important points here. For details of plotting source types on a fundamental lune, the reader is referred to Tape and Tape (2012), Tape and Tape (2013), and references therein.

2.0.1. Source-Type Plots on the Fundamental Lune

Recall that the moment tensor is a 3×3 symmetric matrix. Although the moment tensor quantifies the relative strength of the force couples in the source model, it can also be interpreted as the orientation and source type of a given seismic event. Specifically, a moment tensor $\mathbf{M}$ can be rotated into its principle components via eigen decomposition:

$$\mathbf{M} = \mathbf{U}\Lambda\mathbf{U}^{-1} \tag{2.1}$$

where the columns of the matrix **U** are the eigenvectors with the corresponding eigenvalues in matrix Λ:

$$\Lambda = \begin{bmatrix} \lambda_1 & 0 & 0 \\ 0 & \lambda_2 & 0 \\ 0 & 0 & \lambda_3 \end{bmatrix}. \tag{2.2}$$

In the context of a beachball pattern, the eigenvalues determine the size and pattern of the beachball and the eigenvectors determine its orientation. Note that a single set of eigenvalues $\Lambda = (\lambda_1, \lambda_2, \lambda_3)$ gives a fixed pattern (i.e. source type) of many beachball orientations. In the context of explosion monitoring, this may be sufficient if only the source type is of interest. Thus, to aid in interpretation of source-type, the eigenvalues Λ_M of **M** can be plotted on a portion of the unit sphere and the coordinates of Λ_M can be compared to the coordinates of known source types such as isotropic explosions, earthquakes, or some combination thereof.

A unit sphere $\mathbb{W}$ has coordinates of longitude γ, measured eastwards from $\Lambda = (1, 0, -1)$ direction, and latitude $\delta = \pi/2 - \beta$, where β is the colatitude. The eigenvalues of a given moment tensor are plotted on the sphere $\mathbb{W}$ according to the angles γ and β:

$$\begin{aligned} \tan(\gamma) &= \frac{-\lambda_1 + 2\lambda_2 - \lambda_3}{\sqrt{3}(\lambda_1 - \lambda_3)} \\ \cos(\beta) &= \frac{\lambda_1 + \lambda_2 + \lambda_3}{\sqrt{3}||\Lambda||}, \end{aligned} \tag{2.3}$$

where $||\Lambda||$ is the L^2 norm of Λ;

$$||\Lambda|| = \sum_{i=1}^{3} \sqrt{\lambda_i^2}. \tag{2.4}$$

For arbitrary ordering of the eigenvalues, there are six possible points that the event can plot on the unit sphere $\mathbb{W}$ (see Figure 3 of Tape and Tape (2012)). However, these six points on the unit sphere all have same source mechanism and orientation, so we can reduce geometrical complexity by enforcing the condition $\lambda_1 \geq \lambda_2 \geq \lambda_3$. This forced ordering of the eigenvalues of **M** will confine its location on the unit sphere to a so-called fundamental wedge $\mathbb{L} \in \mathbb{W}$, giving rise to the term fundamental lune. On the fundamental lune $\mathbb{L}$ the longitude γ ranges from $-\pi/6$ to $\pi/6$ and the latitude δ ranges from $-\pi/2$ to $\pi/2$. The latitude δ is zero for deviatoric patterns, while γ and δ are zero for double couple patterns. Isotropic sources have latitude of $\delta = \pm\pi/2$, depending on whether it's an explosion or implosion.

2.0.2. Time Evolution of Source Mechanism

Typically, seismic source-types are plotted on the fundamental lune with the assumption that the STF is identical for all six components of the moment tensor. This assumption, although simplifying the problem and perhaps better constraining the inversion, is an approximation that is not unreasonable for moderately sized earthquakes. Indeed, it is in this context that source-type plots were developed. However, there is an increasing use of the fundamental lune source plot to

discriminate between earthquakes and buried explosions (e.g., (Alvizuri and Tape, 2018; Alvizuri et al., 2018; Chiang et al., 2016, 2018)). However, we argue that the fundamental assumption underlying the use of source-type plots may be missing an important aspect in explosion sources: the time evolution of the source. That is, consider the case where a buried explosion results in a subsequent release of tectonic strain on nearby fractures and/or faults. In this case, the seismic source could be modeled as (nearly) co-located sources, offset in time and type with different STFs. The explosion source would map to the isotropic region of the fundamental lune $\mathbb{L}$ whereas the double couple source related to the slip on the loaded fractures/faults would map to the double couple regions of $\mathbb{L}$. In conventional analysis, these details are completely lost, as the assumptions ensure that the estimated moment tensor is an average of all potential source mechanisms. Indeed, it was under these concerns that we originally developed our time-variable inversion for STFs (e.g. Poppeliers et al. (2019), Poppeliers and Preston (2020b), Poppeliers and Preston (2020a), Poppeliers and Preston (2022)).

Although our time-variable inversion method accounted for potential time-variability of the seismic source mechanisms, it was not easily interpreted. Thus, we combine the results of our inversion with the powerful visualization tool of a fundamental lune source-type plot. By forming a set of eigenvalues for every time point along the six independent STFs, we can form a coordinate in lune space that is a function of time. As a simple test of this concept, in Figure 2-1 we show the STFs for an isotropic explosion and an earthquake. In this simple example, the source types are "pure" in that for a given source type, the STFs are identical and there is no other mechanism present. In this case, because the STFs for each source type are identical, the time-dependent eigenvalues have the same relative magnitude for all time, and thus the trajectory on the corresponding lune plots remains fixed. Note that in this simple example, we did not invert any actual seismic data; rather we simply formed STFs according to equations 1.8 and 1.9, assigned amplitudes to the STFs based on the specific source model's moment tensor, and then for every time point along the STFs formed a six-element tensor and plotted its eigenvalue-derived coordinates on the lune. We did this for both a moment source (SI units = N m) and a moment rate source (SI units = Nms^{-1}). In these plots, we also show the orientation of the mechanism as a beachball pattern for completeness. Interestingly, when performing this analysis on the isotropic-model moment rate STFs, we see a small contraction (small, white, non-filled beachball) at the bottom of the lune (panel C) following the expansion (filled beachball) of the explosion (panel D). This characteristic is due to the simulated explosion STF having a small overshoot that accounts for the slight contraction of the cavity immediately following the explosion and thus represents a small dilatational source type at the end of the explosion STF.

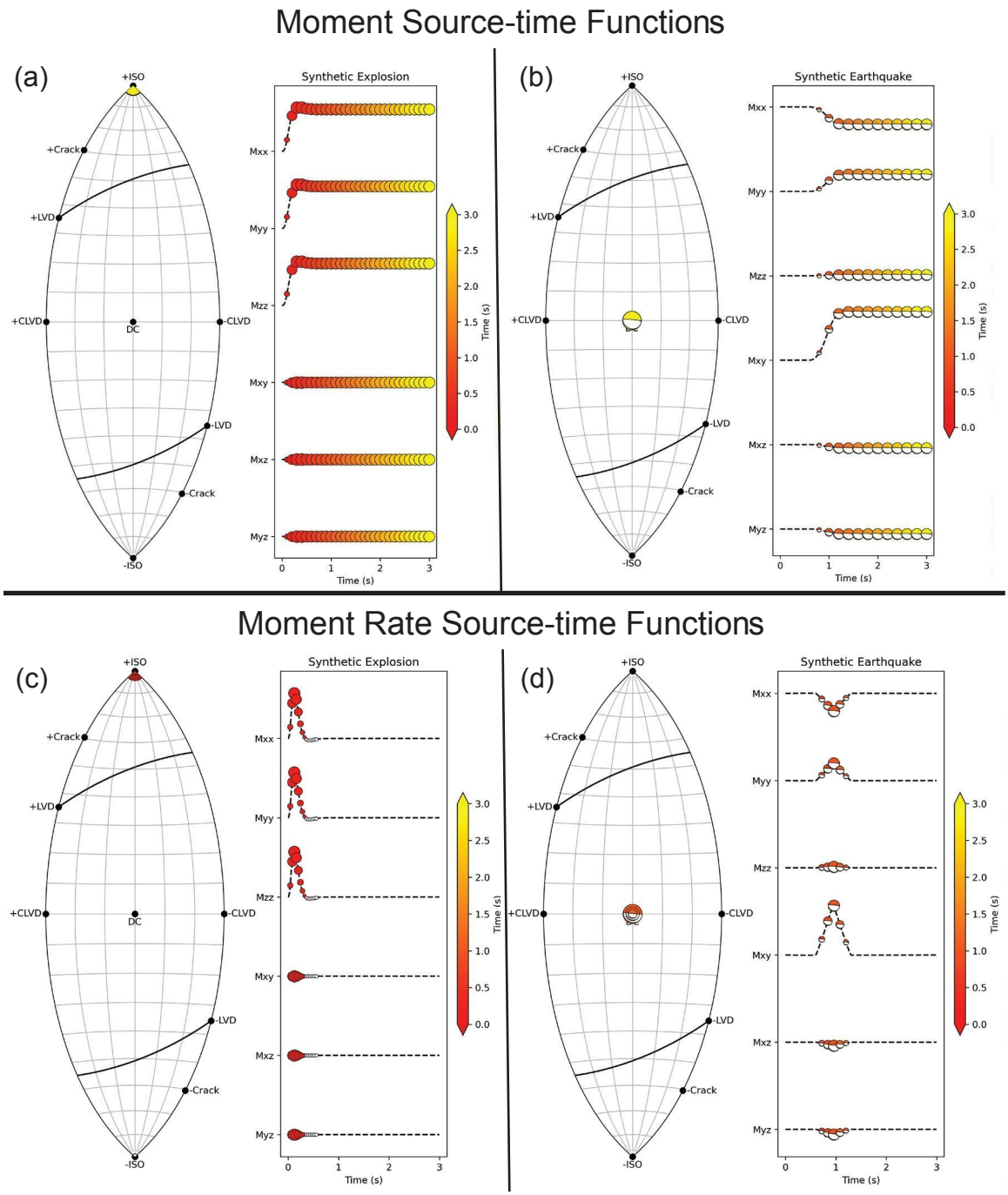

Figure 2-1. Comparing source-type plots with time-variable STFs, for moment STFs (a-b) and moment rate STFs (c-d). Panels (a) and (c) show an explosion mechanism and Panels (b) and (d) show an earthquake mechanism. For this figure, we only show the beachball graphics (in all panels) with the sum of the moment tensor components are greater than 10^{10} N m (panels a and b) or $10^{10} Nms^{-1}$ (panels c and d). For a given time point in the STFs, we form a moment tensor and compute the corresponding beachball graphic and the eigenvalues. We then plot the beachball graphic on the STFs, where its size corresponds to its relative amplitude (equal to the sum of the absolute value of the tensor components for that time). The same beachball mechanisms are plotted according the their eigenvalue coordinates on the lune diagram. Note that for a given source type, the mechanism is the same for all time, and thus all of the points on the lunes overlap. The exception to this is the small implosion mechanism seen in Panel (c), which corresponds to the small overshoot in the explosion source model.

3. EARTH MODEL AND DATA SIMULATION

In order to more completely test our approach, we create synthetic seismic data, invert it according to our time-variable source inversion scheme, and then plot the mechanisms, as a function of time, on the fundamental lune. To create the data, we follow the same procedures as described in Poppeliers and Preston (2020a) and Poppeliers and Preston (2022). That is, we first create an Earth model that consists of a heterogeneous halfspace and compute three-component Green's functions for the six independent components of the moment tensor. Then, by convolving the Green's functions with the appropriate STF, and scaling by an assumed moment tensor, we can form synthetic three-component seismograms for any source model and arrangement of sensors (e.g. equation 1.2).

3.1. Earth Model

The Earth model has physical dimensions of $2500 \times 2500 \times 1500$ m in the x, y, and z directions, respectively, with a discrete node spacing of 10m. The average compressional and shear wavespeeds of the model are 2000 m/s and 1176 m/s, respectively. To introduce semi-realistic scattering effects, we introduce impedance heterogeneities in the form of stochastic perturbations to the wavespeed and density. The heterogeneities follow a von Karman power law decay model, and parameterized with characteristic lengths of $[a_x, a_y, a_z] = [700, 700, 500]$ m with a trimodal distribution of density/wavespeed contrasts of ± 7.5 % about the mean. A slice through the center of the Earth model for the realization of the stochastic model used in our analysis is shown in Figure 3-1. We created a set of arbitrarily-located stations from 150 - 1500 m from the central source (Figure 3-2), where we place the stations 20 m below the top of the model in order to avoid artifacts associated with the finite difference boundary conditions in our wave simulation code. To generate the three-component Green's functions for each station, we use the Sandia-created elastic wave equation simulation code, parelasti. Parelasti uses a second-order time, fourth-order space staggered grid, finite-difference solution to the elastic wave equation to solve for velocity, stress and pressure at each model grid point (Poppeliers and Preston, 2020a).

3.2. Creating Green's Functions and Synthetic Data

We create three-component (3-C) Green's functions (GFs) for each seismic station along the surface of the Earth model space. We use the GFs to create the subsequent seismic data as well as the forward model in our inversion scheme. To account for the Earth-air boundary, we employ a free-surface boundary condition at the top of our Earth model, which given the impedance contrast here, is almost a perfect reflection boundary. To compute a complete suite of 3-C GFs for

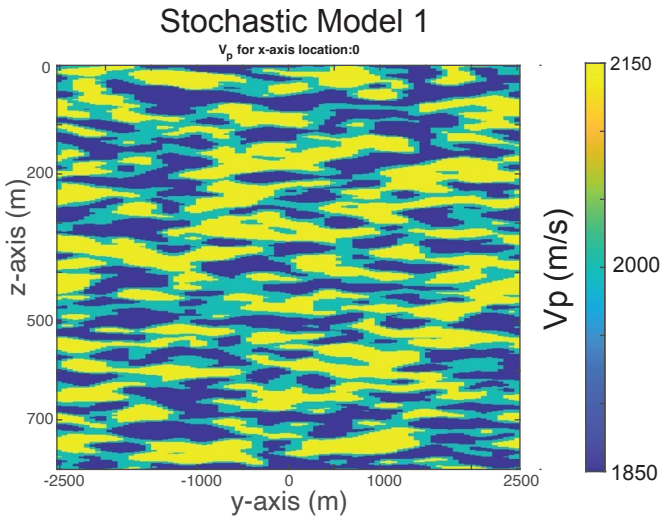

Figure 3-1. 2D Slice (x=0) through the Earth model showing the compressional wavespeed through the realizations of stochastic heterogeneities used in our analysis here.

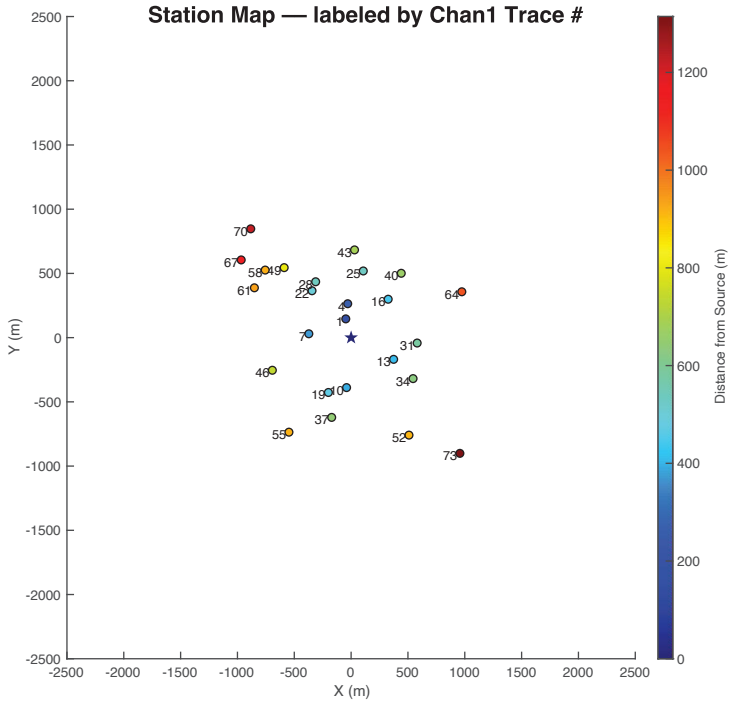

Figure 3-2. Location of stations (on the surface) relative to the source epicenter (star at x = 0 m, y = 0 m). Stations are labeled according to the trace number of the first component; for example, station 1 with 3 components will consist of traces 1-3 but only trace 1 is labeled here.

each seismic station, we define a source location at $[x, y, z] = [0, 0, 300]$ m, where the initial condition is a band-limited delta function. The simulation is run for a model time of 3.0 s, where

the discrete time interval is 0.001 s. Based on the seismic wavespeeds of our model and the discrete time increment, our simulations will produce seismograms that are free from numerical dispersion up to a frequency of approximately 17.5 Hz. To generate the synthetic seismic data in units of velocity (m/s), we solve equation 1.5 for each data component for each station, where we define *apriori* a moment tensor and the corresponding STFs, depending on the source model we wish to simulate.

Let us briefly digress to discuss the importance of the units of the STFs, the data, and what that means for the simulation of the GFs and the seismograms derived with reference to equation 1.5.

1. **Moment STF**: To simulate data with units of velocity (SI units: m/s) from the moment source-time function (units of Nm), then the GFs must be in units of $1/Ns^2$. In the literature, these type of Green's functions are commonly, if not misleadingly, referred to as "velocity Green's functions", although their units are not in velocity. Rather their units are such that when convolved with the appropriate STF (of units of moment) result in velocity seismograms. To prevent confusion on this front, we instead refer to these GFs as $G_{M,V}$ to denote the moment STF and resulting velocity data. Explicitly the units work out as

$$\left[\frac{m}{s}\right]_u = \left[\frac{1}{Ns^2}\right]_{G_{M,V}} [Nm]_h [s]_{dt} \tag{3.1}$$

   where the subscript indicates the quantity with the units designated inside the brackets.

2. **Moment Rate STF**: To simulate velocity data (units of m/s) from the moment rate STF, $\partial h(t)/\partial(t)$ with units of Nms^{-1}, then GFs must be generated with units of $1/Ns$. These GFs are conventionally referred to as "displacement Green's functions" as, when applied with the moment (not moment rate) STF, this results in displacement data. We instead refer to these GFs as $G_{MR,V}$ to prevent confusion in the context of our analysis. Explicitly the units work out as

$$\left[\frac{m}{s}\right]_u = \left[\frac{1}{Ns}\right]_{G_{MR,V}} [\frac{Nm}{s}]_{\partial h(t)/\partial t} [s]_{dt} \tag{3.2}$$

Thus, to obtain synthetic seismic velocity data, we need one set of GFs if using a moment STF ($G_{M,V}$) and another if using a moment-rate STF ($G_{MR,V}$). To obtain the latter we use the -Smr flag in parelasti, but note that the integrated $G_{M,V}$ could also instead be used.

We create three datasets, where the only difference between the three is the source model. For the first set, we assume a pure isotropic explosion where the STF is given by equation 1.8. The second dataset simulates a perfect double-couple earthquake source with a strike, dip, and rake of 10, 85, and 5 degrees, respectively, where the STF is defined by equation 1.9. We show record sections of ground velocity data for both the isotropic explosion (Figure 3-3) and the double-couple earthquake (Figure 3-4) to prove the consistency and validity of generating velocity seismic data using $G_{M,V}$ with moment STFs as compared to that from $G_{MR,V}$ with moment rate STFs. Finally, the third dataset we will explore is formed by combining the two source models: i.e. an isotropic explosion source followed by lower frequency double-couple source with the same strike, dip, and rake as the previous earthquake-only dataset. Each dataset is

computed with units of ground velocity, and all data is inverted by both inversion methods, STF-invariant and STF-Dependent, which we will describe in detail in the following section.

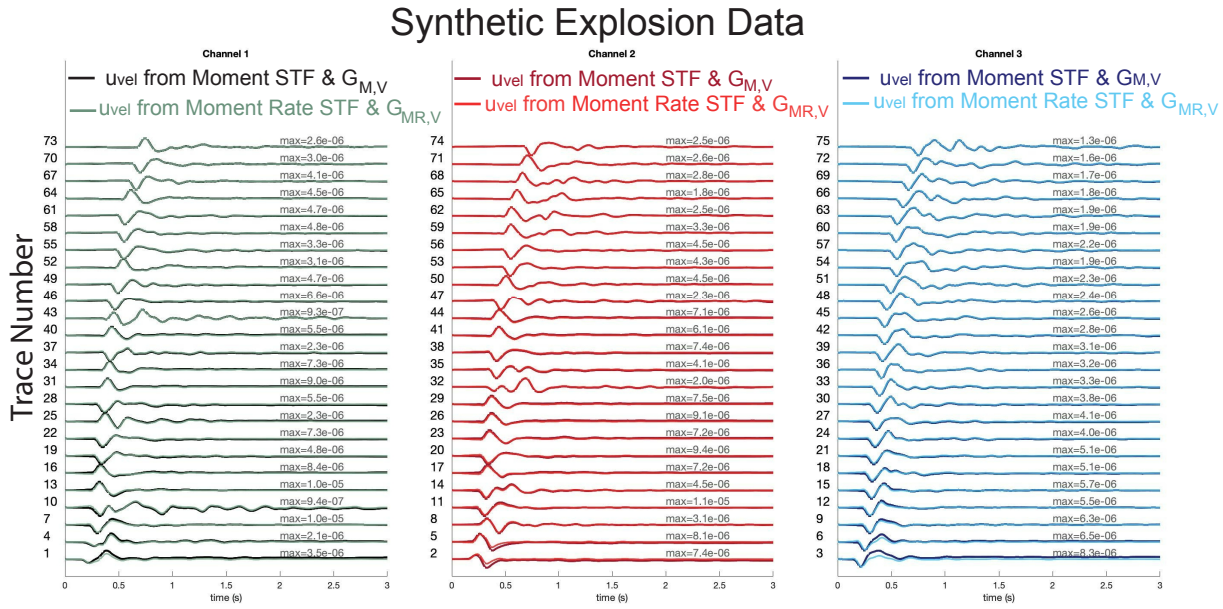

Figure 3-3. Synthetic velocity seismograms for an explosion source, sorted by increasing source-receiver distance showing the comparability between how we generate data from either type of STF and corresponding Green's functions. The y-axis label correspond to the station numbers in Figure 3-2. The three panels correspond to the particle velocity in the $x, y,$ and z directions, respectively. Each seismogram is trace normalized by the data generated from the $MomentSTF$ & $G_{M,V}$.

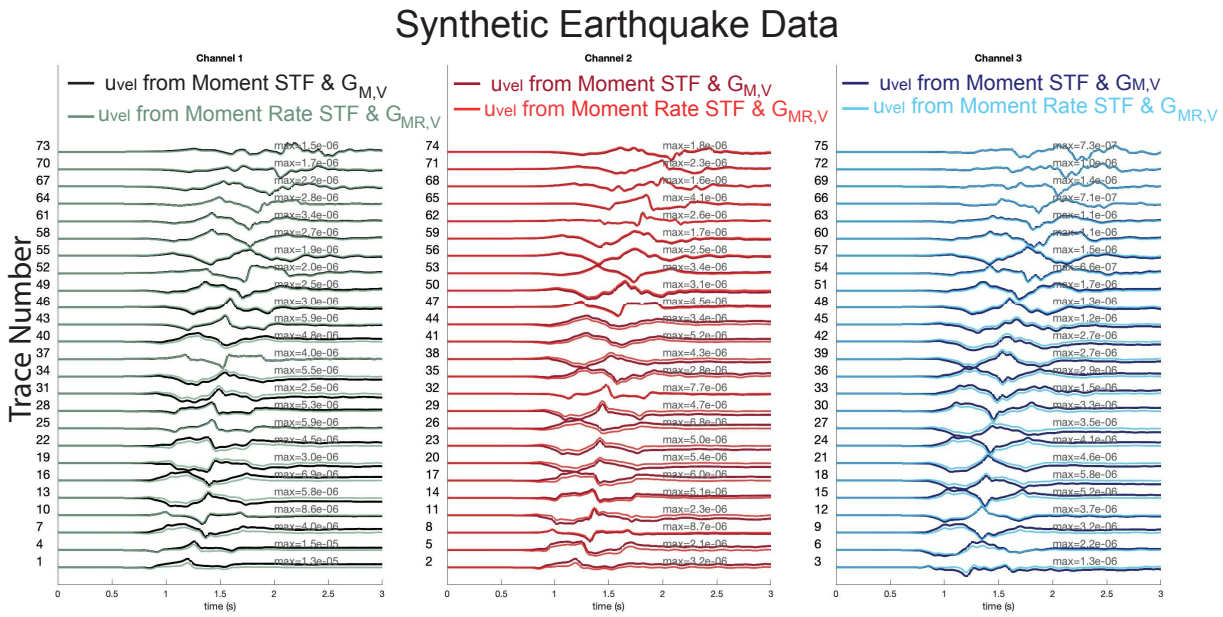

Figure 3-4. Similar to Fig 3-3, but for a synthetic earthquake.

4. INVERSE METHODS AND NUMERICAL TESTS

We explore two types of linear inversions designed to estimate the source parameters. In the first, we use an assumed source function to estimate the scalar values of $\hat{M}_{ij}$. Specifically, we estimate the six scalars corresponding to the six independent components of the moment tensor, $\hat{m}_n$, where we assume an *a priori* STF. We will refer to this inversion scheme as Method 1 STF-Dependent. For Method 1, we also assume that we perfectly know the origin time of the event, as we cannot estimate that from this method. In the second type of inversion, we make no *a priori* assumptions of a STF and instead invert the data for the time-variable STFs $\mathbf{M}_{ij}(t)$, each of which corresponds to a component of the moment tensor. This second inversion scheme, herein denoted Method 2 STF-Invariant, makes no requirement that the STF is similar for all components of the moment tensor. Additionally, Method 2 does not require an *a priori* origin time. In both inversion schemes that we test here, we invert the data to estimate the moment as well as the moment rate functions.

To test the capabilities of both types of inversion we form synthetic data for three types of seismic sources: an isotropic (buried) explosion, a double-couple earthquake, and a combination of the two. We find that for data constructed using only a single source type (i.e. an explosion or double couple source) Method 1 can accurately recover the source parameters of the moment and moment rate functions. However, for the more complex source that consists of a combined explosion and earthquake, Method 2 results in a more accurate estimate of the source parameters, but we find that only the estimated moment rate function capable of completely resolving the independent components of the complex source.

Both methods of inversion are linear, and based on equation 1.3. Specifically, for Method 1, equation 1.4 is recast into a set of linear equations

$$\mathbf{u} = \mathbf{GM} \tag{4.1}$$

where $\mathbf{u}$ and $\mathbf{G}$ are the observed data and the GFs, respectively, and $\mathbf{M}$ are the six scalars corresponding the moment tensor. Note that the GFs are convolved with an *a priori* assumption of a STF, either a moment function or a moment rate function depending on the units of the data. For Method 2, there is no *a priori* assumption about the form of the STF, and thus the GFs are not convolved or filtered in any way prior to construction the system of equations. Note that for both methods, the inversion can be performed in either the time domain or the frequency domain. We will detail both methods of inversion in the next two sections.

4.1. Method 1: Scalar Moment Tensor

Method 1 is the most common method used in the literature, as the problem is both easier to set up, has fewer free parameters, and is arguably appropriate for analyzing low frequency data observed at regional or teleseimic distances. At these scales, the data are typically at too low of a passband to reasonably resolve the detailed time history of the STF and thus the moment rate function is often assumed to be a band-limited delta function or so-called triangle function. While Method 1 can be formulated in the frequency domain, we stay in the time domain so we can directly compare our tests to those commonly used in the literature (e.g. Chiang et al. (2016); Herrmann et al. (2011); Herrmann (2013)). Specifically, the time-domain formulation is given as

$$\begin{bmatrix} | \\ u_1(t) \\ | \\ | \\ u_2(t) \\ | \\ \vdots \\ | \\ u_K(t) \\ | \end{bmatrix}_{TK\times 1} = \begin{bmatrix} | & | & & | \\ \hat{\mathbf{G}}_{1,1}(t) & \hat{\mathbf{G}}_{1,1}(t) & \dots & \hat{\mathbf{G}}_{1,N}(t) \\ | & | & & | \\ | & | & & | \\ \hat{\mathbf{G}}(t)_{2,1} & \hat{\mathbf{G}}(t)_{2,2} & \dots & \hat{\mathbf{G}}(t)_{2,N} \\ | & | & & | \\ | & | & & | \\ \hat{\mathbf{G}}(t)_{3,1} & \hat{\mathbf{G}}(t)_{3,2} & \dots & \hat{\mathbf{G}}(t)_{3,N} \\ | & | & & | \\ \vdots & \vdots & \ddots & \vdots \\ | & | & & | \\ \hat{\mathbf{G}}(t)_{K,1} & \hat{\mathbf{G}}(t)_{K,2} & \dots & \hat{\mathbf{G}}(t)_{K,N} \\ | & | & & | \end{bmatrix}_{TK\times N} \begin{bmatrix} M_1 \\ M_2 \\ \vdots \\ M_N \end{bmatrix}_{N\times 1} \tag{4.2}$$

where $[-u_k(t)-]^T$ is the observed time domain data (of length T) for channel k (of which there are K) and M_n is a scalar corresponding to the n^{th} moment tensor component (up to $n = 6$ total terms). The term $[-\hat{\mathbf{G}}(t)_{k,n}-]^T$ is the time domain GF for channel k and moment tensor component n that has been convolved with an *a priori* assumption of an STF. We use velocity seismic data and the corresponding GFs to estimate moment and moment-rate tensor components. Specifically, to estimate the moment rate tensor scalar components,

$$\hat{\mathbf{G}}_{k,n}(t) = \int_{-\infty}^{\infty} \mathbf{G}_{MR,V_{k,n}}(t) \frac{\partial h(t)}{\partial t} dt \tag{4.3}$$

where the subscript MR,V indicates that the units of the GF, when convolved with the moment rate function $\frac{\partial h(t)}{\partial t}$, will result in the quantity $\hat{\mathbf{G}}_{k,n}(t)$, which predicts the velocity seismograms according to equation 1.5. Similarly, if we aim to estimate the moment tensor scalar components, then

$$\hat{\mathbf{G}}_{k,n}(t) = \int_{-\infty}^{\infty} \mathbf{G}_{M,V_{k,n}}(t) h(t) dt. \tag{4.4}$$

4.1.1. Numerical Tests

Recall that we constructed three datasets, one for three source models: an explosion, an earthquake, and a combined source consisting of an earthquake followed by an explosion. We invert these data according to the scheme described in equation 4.2. After inverting, we obtain the estimated scalar terms of the moment tensor M_n which we can use to determine the source type (equations 2.1-2.4) as well as to form predicted data according to equation 1.5.

We show the results from inverting the first two datasets, for an explosion and for an earthquake, to estimate the moment and moment rate scalar values in Figures 4-1 and 4-2, respectively. We compute the L2 misfit to quantify the fit-to-data for each inversion (Poppeliers and Preston, 2020b). From these figures we see that the data are all able to be fit using this inversion scheme, which proves the capability of our inversion to estimate moment and moment rate scalar tensor values. However, we also observe that the fit-to-data appear better in our inversion to estimate moment rate scalar values (Figure 4-2). This is most likely due to the fact that the moment rate function has compact support, meaning the value of the function begins and ends at zero, which appears to result in a better constrained inversion. The lune plots show the estimated source mechanism, which is estimated for the explosion data and the earthquake data in both Figures 4-1 and 4-2.

Similarly, for our more complex source, an earthquake followed by an explosion, we display the results from our inversions to estimate the moment and moment rate scalar values in Figures 4-3 and 4-4, respectively. An immediate observation is that the the L2 misfit for the single-source source models (i.e. the explosion- and earthquake-source models), indicated in panels (a) and (b) of Figures 4-1 and 4-2, is very low whereas the misfit is significantly higher for the case when the source consisted of an earthquake followed by an explosion, as seen in Figures 4-3 and 4-4. This is not surprising as the inversion Method 1 is not able to estimate this time variable source type, rather it finds the best solution that essentially averages the two source types, resulting in a source estimate that imperfectly predicts the data. We also show the estimated source mechanism for the combined explosion/earthquake data on the lune (see Figures 4-3 and 4-4), which plots as a point between the double-couple and explosion points for both the estimated moment and moment rate scalar values. Note that the lune coordinates, although not totally incorrect given the combined nature of the source, does not give any insight into the time evolution of the source mechanism.

4.2. Method 2: Estimating Time-Variable Moment Tensor

Method 2, although a linear inversion scheme, makes no *a priori* assumptions concerning the STF, other than it being localized in space. Specifically, each component of the moment tensor is allowed to have independent time histories. This method may be more appropriate for analyzing underground explosions at higher frequencies, as these source types are often of a combination of an explosion and near-source shear sources. The inversion scheme can be formulated in either the time or frequency domains. Poppeliers & Preston (2019, 2020) describe a method to formulate the inversion in the frequency domain, as it is computationally far less demanding than a time domain

formulation. Specifically, the frequency domain implementation of inversion Method 2 is

$$\begin{bmatrix} | \\ u_1(f) \\ | \\ | \\ u_2(f) \\ | \\ \vdots \\ | \\ u_K(f) \\ | \end{bmatrix}_{FK\times 1} = \begin{bmatrix} [\mathbf{G}_{1,1}] & [\mathbf{G}_{1,2}] & \dots & [\mathbf{G}_{1,N}] \\ [\mathbf{G}_{2,1}] & [\mathbf{G}_{2,2}] & \dots & [\mathbf{G}_{2,N}] \\ [\mathbf{G}_{3,1}] & [\mathbf{G}_{3,2}] & \dots & [\mathbf{G}_{3,N}] \\ \vdots & \vdots & \ddots & \vdots \\ [\mathbf{G}_{K,1}] & [\mathbf{G}_{K,2}] & \dots & [\mathbf{G}_{K,N}] \end{bmatrix}_{FK\times NF} \begin{bmatrix} | \\ M_1(f) \\ | \\ | \\ M_2(f) \\ | \\ \vdots \\ | \\ M_N(f) \\ | \end{bmatrix}_{NF\times 1} \tag{4.5}$$

where f is frequency, of which there are F, and

$$\mathbf{G}_{k,n} = \begin{bmatrix} G_{k,n}(f_1) & \dots & 0 \\ \vdots & \searrow & \vdots \\ 0 & \dots & G_{k,n}(f_F) \end{bmatrix} \tag{4.6}$$

is an $F \times F$ diagonal matrix containing the frequency domain Green's function for the k^{th} receiver channel and the n^{th} source type. Note that in this inversion method, the GF is not convolved with any *a priori* assumed STFs, as the inversion will estimate these directly for each component of the moment tensor. After Fourier transforming the observed data and GFs, the system of equations shown in 4.5 is solved for $M_N(f)$ and transformed into the time domain via the inverse Fourier transform (not forgetting to scale by $1/dt$ to account for the dt term in the convolution). Similar to the inversion Method 1, we use Green's functions with appropriate units to estimate the moment and moment rate source time-series. After estimating the time-variable moment tensor components as functions of time $m_n(\mathbf{x},t)$, we use equation 1.2 to compute the predicted data.

Akin to our previously presented results, we show the results from our inversion of singular sources, including an explosion and an earthquake, from velocity seismic data to estimate moment and moment rate in Figures 4-5 and 4-6. However, because the source model has time-variable behavior we add an additional column that shows the time-variable STF corresponding to the moment tensor with the estimated source mechanism plotted as a beachball directly on the STF time series. We see that the single-source models (the explosion in panel (a) and the earthquake in panel (b)) are accurately estimated with a correspondingly low degree of misfit. We also consider the estimated results from the more complex source of an earthquake followed by an explosion for both moment and moment rate as functions of time in Figures 4-7 and 4-8. In this case, we observe that the estimated moment tensor functions still struggle to fully separate the explosion following the earthquake source as evidenced on the lune. However, the

estimated moment rate tensor functions are able to resolve the independent sources with two clusters located at the double-couple earthquake and the isotropic explosion in lune coordinates and as evidenced by the beachball graphics.

Estimated Moment Scalar Values from STF-Dependent Inversion

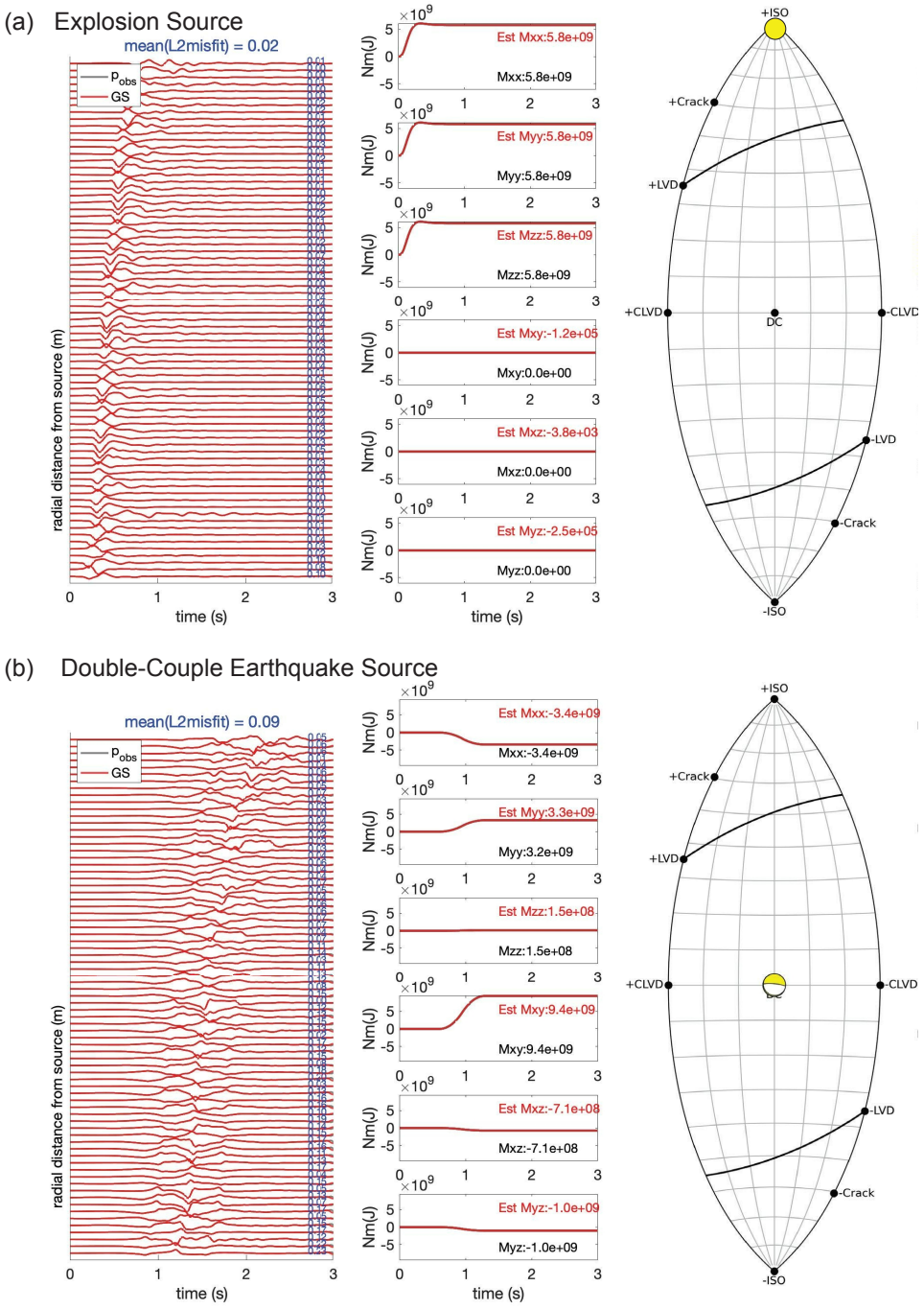

Figure 4-1. Results of inverting the two velocity datasets with a singular source, where the STF is a moment function $h(t)$ using inversion Method 1: (a) the explosion-only data , and (b), the earthquake-only data. The left-hand columns show the observed (synthetic) seismic data (black) and predicted data (red), organized from nearest to the source on the bottom to furthest on top, where the total data misfit is indicated above the data . The observed and predicted data are filtered to 1-15Hz passband. In the center column we show the time-series of the moment sources from the *a priori* STF convolved with the true scalar values (grey), and convolved with the estimated scalar values resulting form the inversion (red). The right-hand column shows the estimated moment tensor scalar values plotted on the fundamental lune, where the source mechanism and orientation are indicated by the beach-ball graphic.

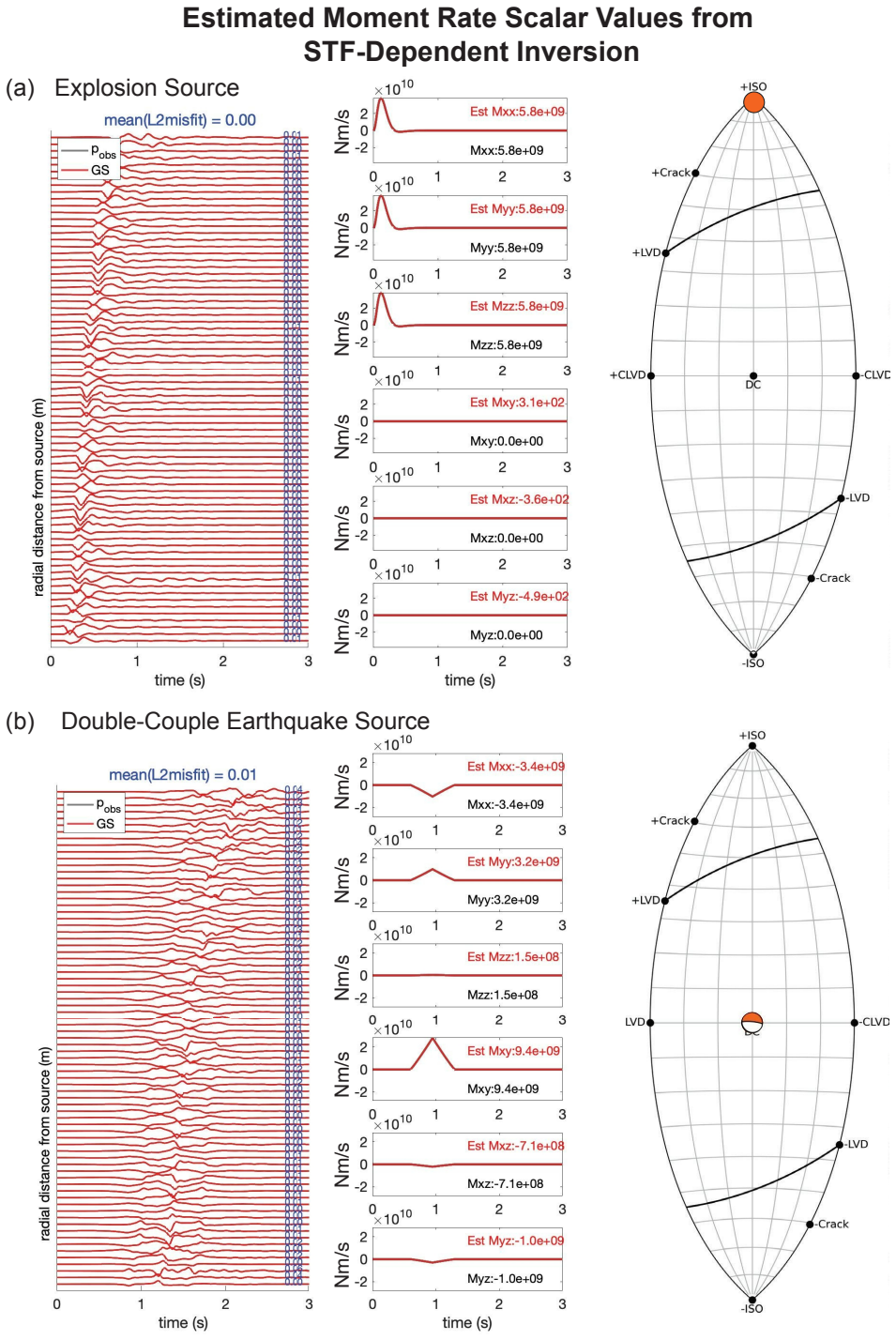

Figure 4-2. Similar to Figure 4-1 except the inversion estimates the scalar values associated with the moment rate, $\partial h(t)/\partial t$.

Estimated Moment Scalar Values from STF-Dependent Inversion

(a) Earthquake followed by Explosion

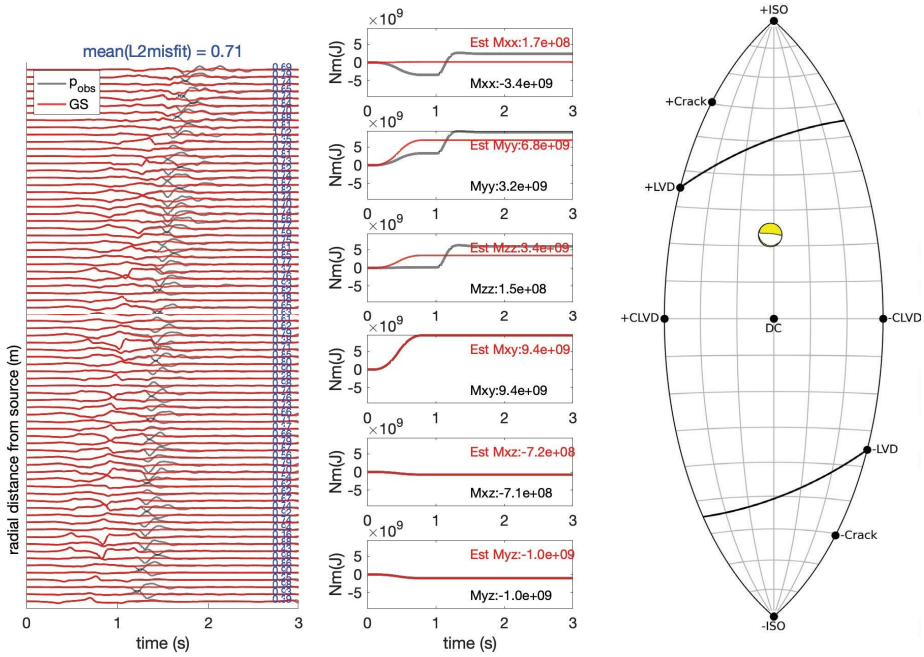

Figure 4-3. Similar to Figure 4-1 except the inversion estimates the scalar values of the moment, $h(t)$ from velocity data of an explosion followed by an earthquake.

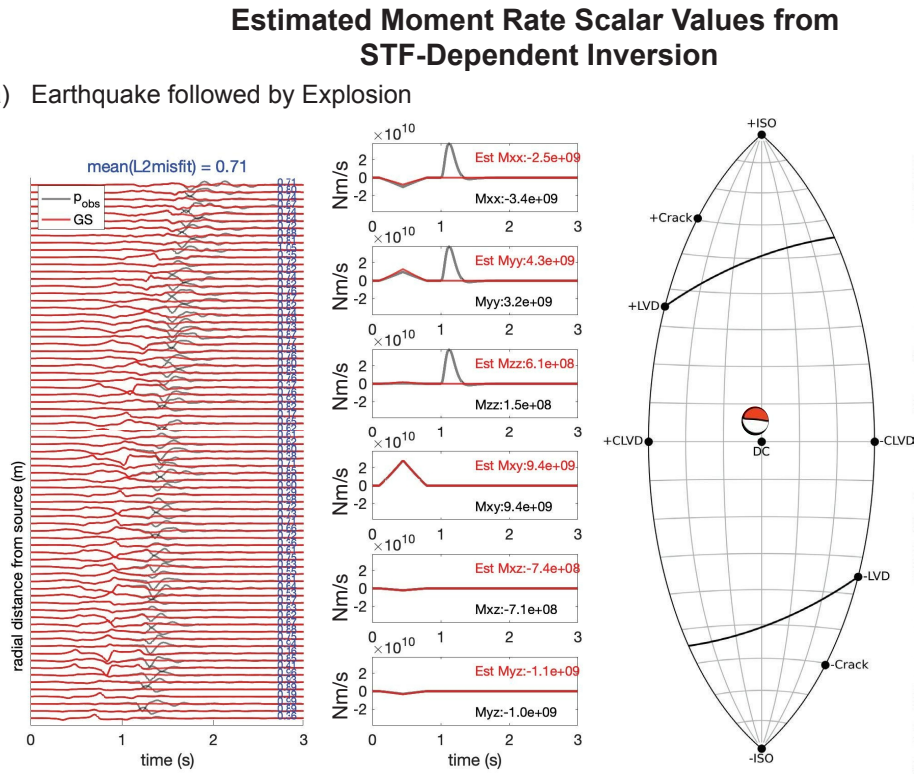

Figure 4-4. Similar to Figure 4-3 except the inversion estimates the scalar values associated with the moment rate.

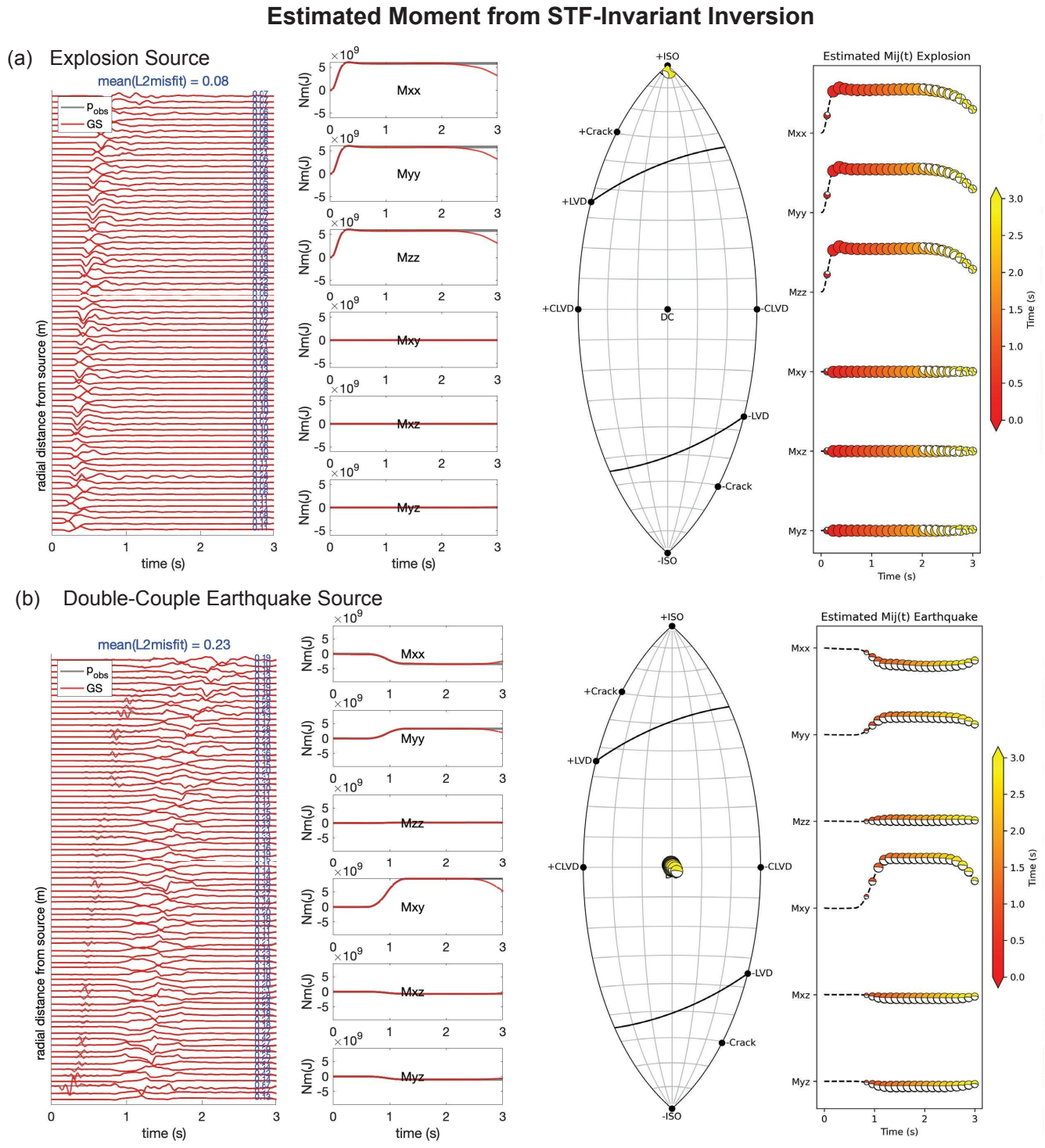

Figure 4-5. Results from inversion to estimate time-variable moment source parameters for an (a) explosion source and (b) earthquake source.

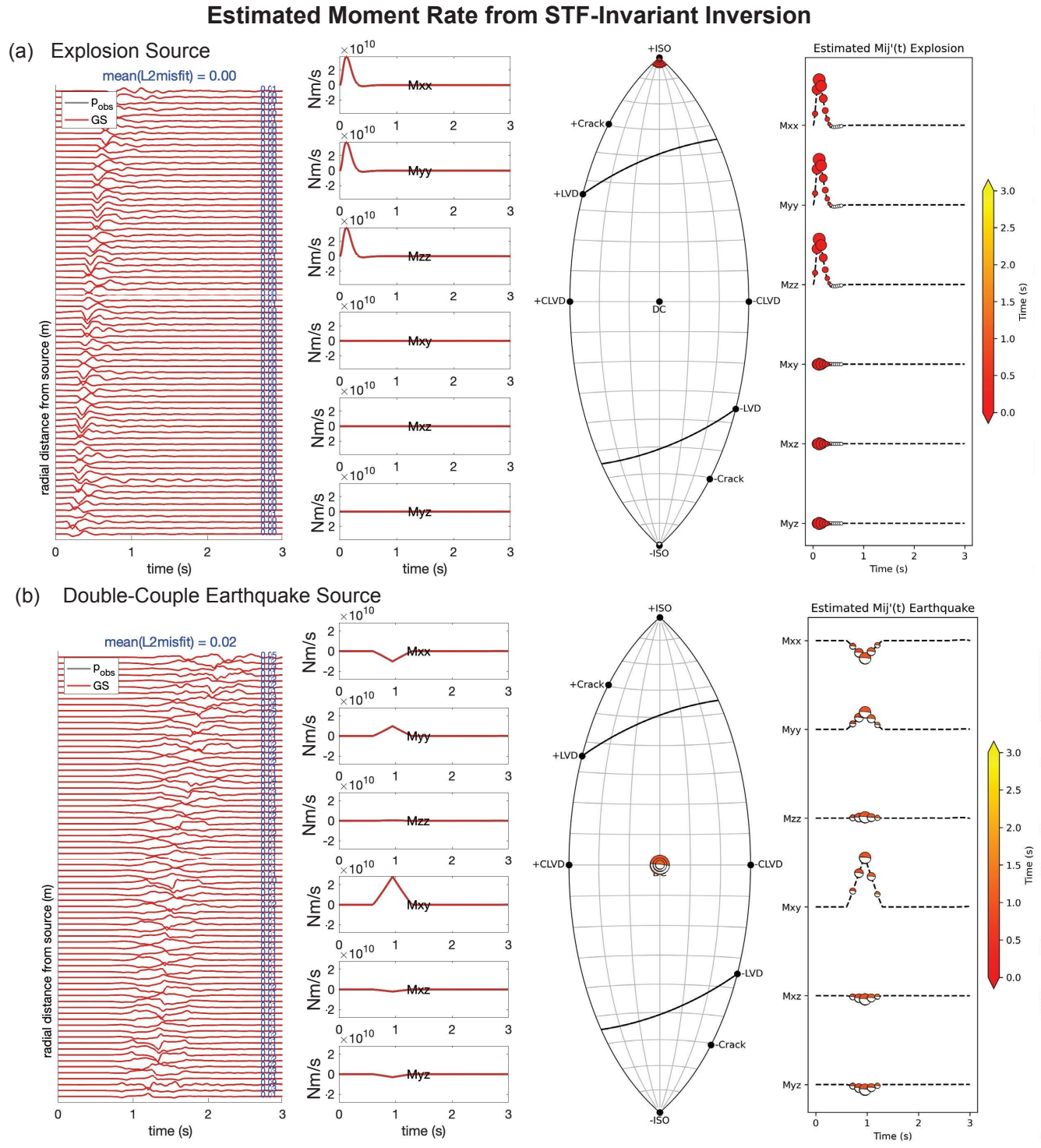

Figure 4-6. Similar to Figure 4-5 except the inversion estimates the time-variable moment rate source parameters.

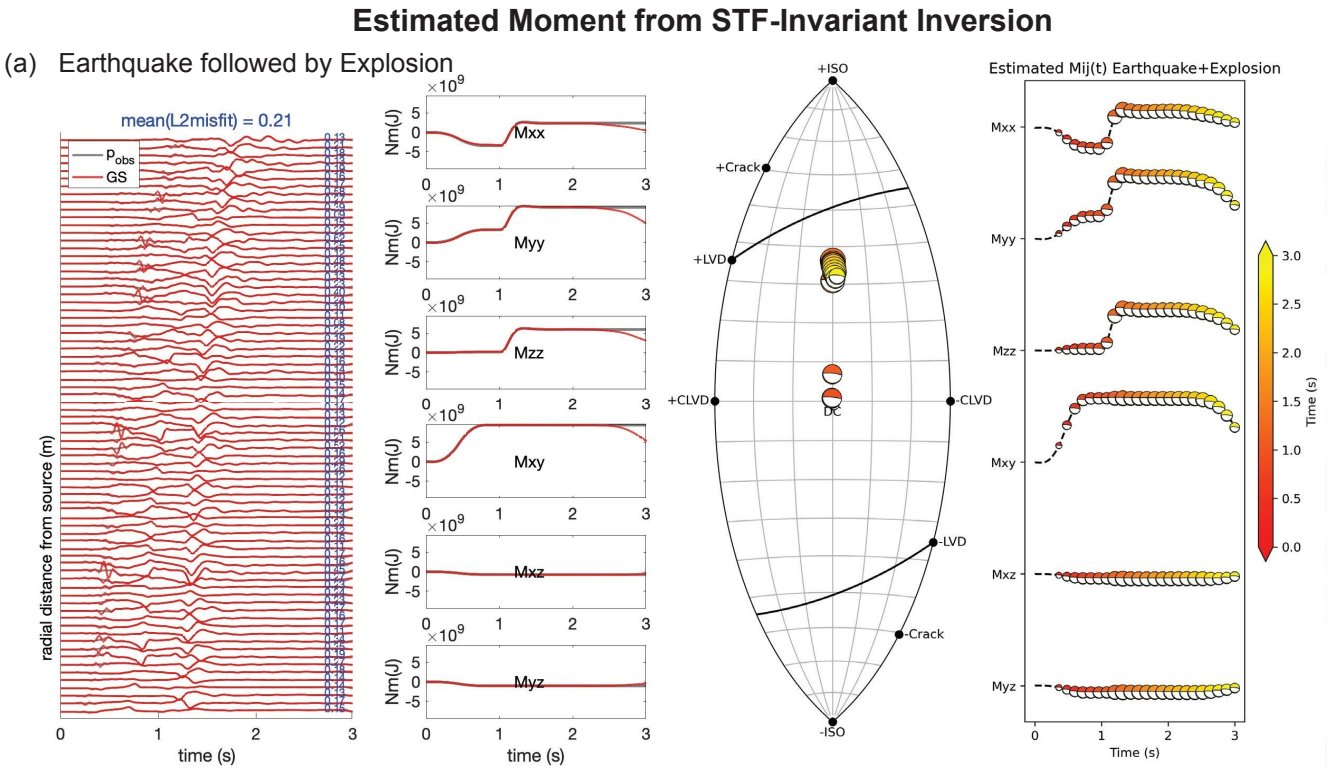

Figure 4-7. Results from inversion to estimate time-variable moment source parameters from velocity data created from complex sources of an earthquake followed by an explosion.

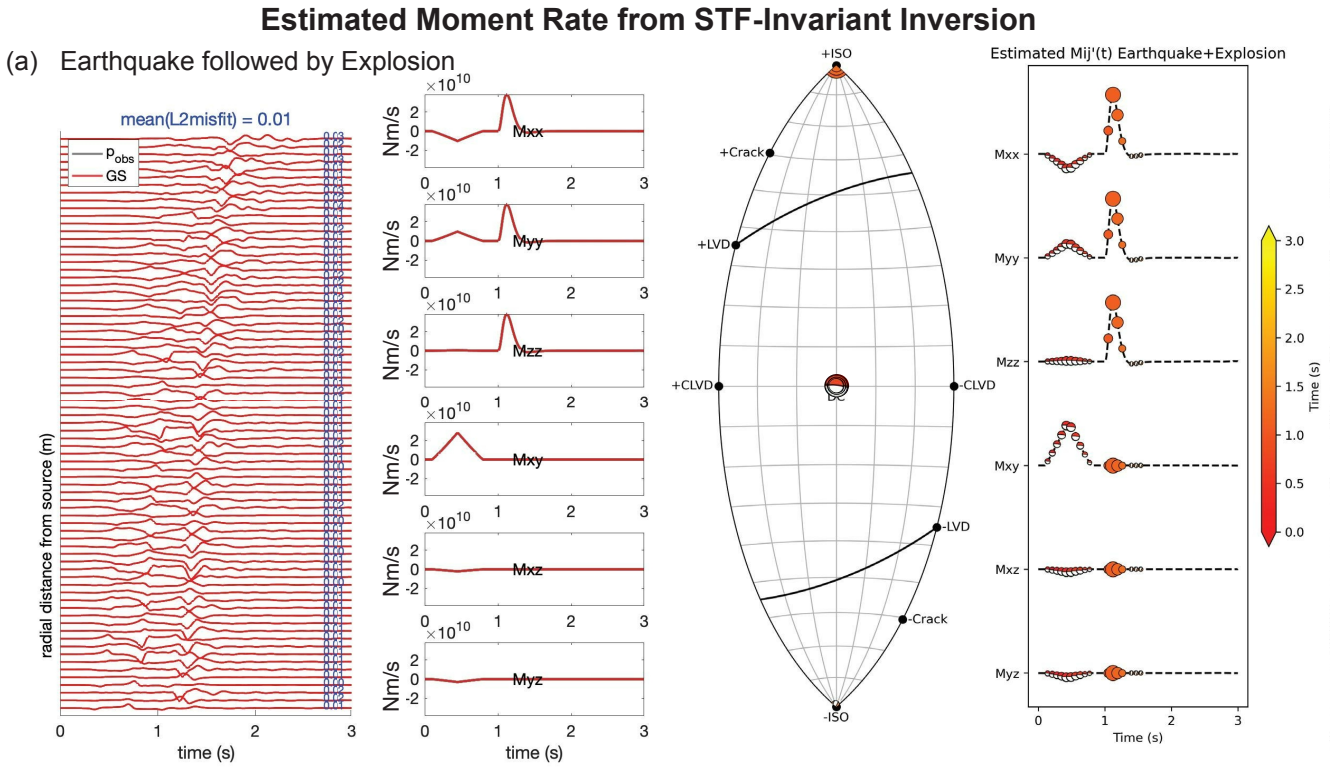

Figure 4-8. Similar to Figure 4-7, but results from the inversion to estimate time-variable moment rate source parameters.

5. CONCLUSIONS

We present two inversion types: Method 1. estimate source scalar values with *a priori* STFs (STF-Dependent) and Method 2. estimate the time-series source parameters without *a priori* STFs (STF-Invariant). We investigate both inversion methods to resolve the moment and moment rate source parameters as scalars, Method 1, and functions of time, Method 2. While all inversion methods and estimated sources are able to accurately resolve singular sources of an earthquake or an explosion, only by performing the Method 2 inversion scheme and resolving for the moment-rate parameters, as functions of time, are we able to constrain a complex, multi-phenomenology source consisting of an earthquake followed by an explosion. To visualize the STFs, we decompose these into time-evolving beachball graphics onto a fundamental lune to convey both orientation and source type. We note that while the Method 2 inversion scheme is able to resolve complex sources in our ideal, synthetic case, this method may also be more sensitive to noise and/or uncertainty in the earth model and recorded seismic data. We do not explore the extent that this may persist within this analysis, but will explore that in future work. Additionally, we will apply our investigation to invert recorded seismic data to constrain real-world sources.

REFERENCES

Aki, K. and Richards, P. G. (2002). *Quantitative seismology*. University Science Books, 2 edition.

Alvizuri, C., Silwal, V., Krischer, L., and Tape, C. (2018). Estimation of Full Moment Tensors, Including Uncertainties, for Nuclear Explosions, Volcanic Events, and Earthquakes. *Journal of Geophysical Research: Solid Earth*, 123(6):5099–5119. _eprint: https://agupubs.onlinelibrary.wiley.com/doi/pdf/10.1029/2017JB015325.

Alvizuri, C. and Tape, C. (2018). Full Moment Tensor Analysis of Nuclear Explosions in North Korea. *Seismological Research Letters*, 89(6):2139–2151. _eprint: https://pubs.geoscienceworld.org/ssa/srl/article-pdf/89/6/2139/4536951/srl-2018158.1.pdf.

Ammon, C. J., Velasco, A. A., Lay, T., and Wallace, T. C. (2020). *Foundations of modern global seismology*. Academic Press.

Chiang, A., Dregar, D. S., Ford, S. R., Walter, W. R., and Yoo, S.-H. (2016). Moment tensor analysis of very shallow sources. *Bulletin of the Seismological Society of America*, 106(6):2436–2449. Number: 6.

Chiang, A., Ichinose, G. A., Dreger, D. S., Ford, S. R., Matzel, E. M., Myers, S. C., and Walter, W. R. (2018). Moment Tensor Source-Type Analysis for the Democratic People's Republic of Korea–Declared Nuclear Explosions (2006–2017) and 3 September 2017 Collapse Event. *Seismological Research Letters*, 89(6):2152–2165. _eprint: https://pubs.geoscienceworld.org/ssa/srl/article-pdf/89/6/2152/4536860/srl-2018130.1.pdf.

Ford, S. R., Dreger, D. S., and Walter, W. R. (2009). Source analysis of the Memorial Day explosion, Kimchaek, North Korea. *Geophysical Research Letters*, 36(21). Publisher: John Wiley & Sons, Ltd.

Haskell, N. A. (1967). Analytic approximation for the elastic radiation from a contained underground explosion. *Journal of Geophysical Research (1896-1977)*, 72(10):2583–2587. _eprint: https://agupubs.onlinelibrary.wiley.com/doi/pdf/10.1029/JZ072i010p02583.

Herrmann, R. B. (2013). Computer Programs in Seismology: An Evolving Tool for Instruction and Research. *Seismological Research Letters*, 84(6):1081–1088. _eprint: https://pubs.geoscienceworld.org/ssa/srl/article-pdf/84/6/1081/2766621/1081.pdf.

Herrmann, R. B., Benz, H., and Ammon, C. J. (2011). Monitoring the Earthquake Source Process in North America. *Bulletin of the Seismological Society of America*, 101(6):2609–2625. _eprint: https://pubs.geoscienceworld.org/ssa/bssa/article-pdf/101/6/2609/2655813/2609.pdf.

Hudson, J. A., Pearce, R. G., and Rogers, R. M. (1989). Source type plot for inversion of the moment tensor. *Journal of Geophysical Research: Solid Earth*, 94(B1):765–774. _eprint: https://agupubs.onlinelibrary.wiley.com/doi/pdf/10.1029/JB094iB01p00765.

Mueller, R. A. and Murphy, J. R. (1971). Seismic characteristics of underground nuclear detonations: Part I. Seismic spectrum scaling. *Bulletin of the Seismological Society of America*, 61(6):1675–1692.

Murphy, J. R. (1977). Seismic source functions and magnitude determinations for underground nuclear detonations. *Bulletin of the Seismological Society of America*, 67(1):135–158.

Poppeliers, C., Anderson Au, K., and Preson, L. (2019). The Relative Importance of Assumed Infrasound Source Terms and Effects of Atmospheric Models on the Linear Inversion of Infrasound Time Series at the Source Physics Experiment. *Bulletin of the Seismological Society of Amercia*, 109(1):463–475.

Poppeliers, C. and Preston, L. (2020a). The effects of earth model uncertainty on the inversion of seismic data for seismic source functions. *Geophysical Journal International*, 224(1):100–120. _eprint: https://academic.oup.com/gji/article-pdf/224/1/100/34193325/ggaa408.pdf.

Poppeliers, C. and Preston, L. (2020b). Inverting infrasound data for the seismoacoustic source time functions and surface spall at the Source Physics Experiments Phase II: Dry Alluvium Geology. *SANDReport*.

Poppeliers, C. and Preston, L. (2022). An efficient method to propagate model uncertainty when inverting seismic data for time domain seismic moment tensors. *Geophysical Journal International*. _eprint: https://academic.oup.com/gji/advance-article-pdf/doi/10.1093/gji/ggac227/44112103/ggac227.pdf.

Rösler, B. and Stein, S. (2022). Consistency of Non-Double-Couple Components of Seismic Moment Tensors with Earthquake Magnitude and Mechanism. *Seismological Research Letters*.

Tanioka, Y. and Ruff, L. J. (1997). Source Time Functions. *Seismological Research Letters*, 68(3):386–400. _eprint: https://pubs.geoscienceworld.org/ssa/srl/article-pdf/68/3/386/2753651/srl068003_0386.pdf.

Tape, W. and Tape, C. (2012). A geometric setting for moment tensors. *Geophysical Journal International*, 190(1):476–498. _eprint: https://academic.oup.com/gji/article-pdf/190/1/476/1631719/190-1-476.pdf.

Tape, W. and Tape, C. (2013). The classical model for moment tensors. *Geophysical Journal International*, 195(3):1701–1720. _eprint: https://academic.oup.com/gji/article-pdf/195/3/1701/17052523/ggt302.pdf.

Werth, G. C. and Herbst, R. F. (1963). Comparison of amplitudes of seismic waves from nuclear explosions in four mediums. *Journal of Geophysical Research (1896-1977)*, 68(5):1463–1475. _eprint: https://agupubs.onlinelibrary.wiley.com/doi/pdf/10.1029/JZ068i005p01463.

DISTRIBUTION

Hardcopy—External

Number of Copies	Name(s)	Company Name and Company Mailing Address
n/a	n/a	

Hardcopy—Internal

Number of Copies	Name	Org.	Mailstop
1	Elizabeth Berg	6756	0404
1	Christian Poppeliers	8911	0750
1	Kyle R. Jones	8911	0735
1	Stephanie Teich-McGoldrick	6756	0404

Email—Internal (encrypt for OUO)

Name	Org.	Sandia Email Address
Technical Library	1911	sanddocs@sandia.gov

Sandia National Laboratories is a multimission laboratory managed and operated by National Technology & Engineering Solutions of Sandia LLC, a wholly owned subsidiary of Honeywell International Inc., for the U.S. Department of Energy's National Nuclear Security Administration under contract DE-NA0003525.